Preprint typeset in JINST style - HYPER VERSION

Neutron assay in mixed radiation fields with a ^{6}Li-loaded plastic scintillator

M. J. I. Balmer[a]*, K. A. A. Gamage[a] and G. C. Taylor[b]

[a] *Department of Engineering,*
Lancaster University, LA1 4YW, UK
[b] *Neutron Metrology Group, National Physical Laboratory*
Teddington, TW11 0LW, UK
E-mail: m.balmer@lancaster.ac.uk

ABSTRACT: A novel technique for assay of thermal and fast neutrons in a ^{6}Li-loaded plastic scintillator is presented. Existing capture-gated thermal neutron detection techniques were evaluated with the ^{6}Li-loaded plastic scintillator studied in this work. Using simulations and experimental work, shortcomings in its performance were highlighted. As a result, it was proposed that by separating the combined fast and thermal neutron events from gamma events, using established pulse shape discrimination techniques, the thermal neutron events could then be assayed. Experiments were conducted at the National Physical Laboratory, Teddington, performing neutron assays with seven different neutron fields using the proposed technique. For each field, thermal and fast neutron content was estimated and were shown to corroborate with the seven synthesised fields.

KEYWORDS: Neutron detectors (cold, thermal, fast neutrons); Instrumentation for neutron sources; Scintillators, scintillation and light emission processes (solid, gas and liquid scintillators); Pattern recognition, cluster finding, calibration and fitting method.

*Corresponding author.

Contents

1. Introduction

It is highly desirable to detect both fast and thermal neutrons, in order to perform accurate neutron dosimetry in an energy distributed field. Using a liquid scintillator with current state-of-the-art pulse shape discrimination techniques (PSD), neutron interactions in the detector can be discriminated from gamma interactions down to around 40 keVee [1]. This equates to a neutron energy of approximately 450 keV, although this is dependent on a number of factors including detector dimensions and type of scintillant [2].

Figure 1 shows three neutron spectra of different workplace fields. It can be seen that energies below 450 keV account for the majority of the neutron fluence in these fields. Not being able to detect neutron fluences at these lower energies would likely lead to an inaccurate estimate of the dose of these fields (despite the conversion coefficients being substantially lower below 450 keV than above 450 keV). Therefore, it is of great importance for accurate neutron dosimetry, to be able to quantify the contents of this region by determining the thermal content within the field.

Traditionally, ^{3}He based detectors have been used for thermal neutron detection. However, dwindling ^{3}He stocks mean that there is an ever present need to identify alternatives for these detectors [5]. A scintillator loaded with a high neutron capture cross-section isotope such as ^{10}B, ^{6}Li or gadolinium allows the extension of neutron detection below the 450 keV limit imposed by a typical non-loaded liquid organic scintillator, whilst still being able to detect fast neutron interactions. With a high neutron capture cross section, ^{10}B-loaded scintillators have been extensively used for thermal neutron detection [6, 7, 8, 9, 10, 11]. These scintillators are typically loaded with up to 5%

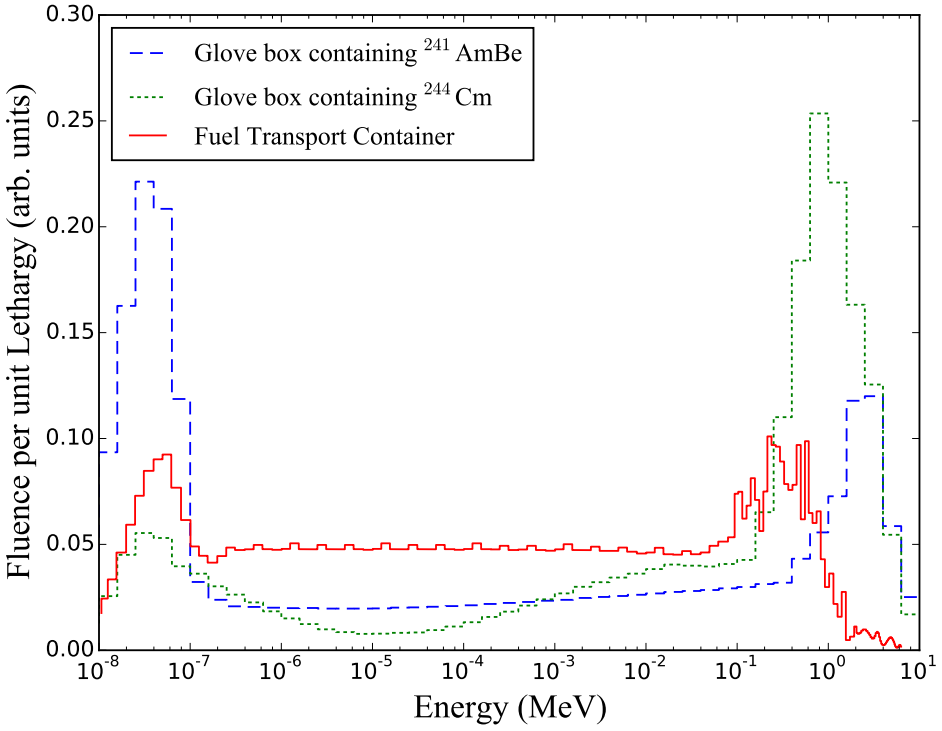

Figure 1. Three typical energy-distributed neutron workplace fields [3, 4]. The importance of detecting both thermal and fast neutrons to allow accurate neutron dosimetry of this field can seen.

fractional mass of ^{10}B. The ^{10}B capture reaction for 6% branching ratio and 94% branching ratio are shown in equation 1.1 and equation 1.2 respectively.

$$^{1}n + \ ^{10}B - > \ ^{7}Li\,(0.84\,MeV) + ^{4}He\,(1.47\,MeV) \tag{1.1}$$

$$^{1}n + \ ^{10}B - > \ ^{7}Li + ^{4}He + \gamma\,(0.477\,MeV) \tag{1.2}$$

Although equation 1.1 shows a high energy ^{4}He, emitted as a result of capture, in practice it has been observed that a strong quenching of the scintillation event leads to a detected pulse of around 60 keVee with the commericially available BC523A [11]. Further developments of ^{10}B-loaded liquid scintillators have increased this to 100 keVee with the scintillator EJ309B5 [12]. The 60 keVee neutron capture signal lies beneath the region of efficient pulse shape discrimination for most liquid scinitillators. As such, a capture gating technique is used to discriminate the neutron capture pulses from gamma or fast neutron interactions [6, 10]. Capture gating relies on detecting both the recoil and capture of a single neutron within the scintillator. When the detector is triggered, a time window is applied, during which time detection of two events leads to the assumption of a possible neutron capture.

To achieve a high efficiency with capture gated detection, a number of considerations must be given. The volume of the detector must be sufficiently large to allow multiple neutron interactions

in the scintillator before capture, so that the resulting pulse is of a detectable amplitude. The trigger threshold for the neutron recoil pulse must also be considered. A low trigger threshold not only increases the processing demands on the electronics system (due to more frequent triggering), but also increases the probability of detecting an unwanted *accidental*, i.e. a gamma interaction. A significant potential advantage of capture gated detection is that neutron capture detection could be possible without any pulse shape discrimination or pulse height information. By simply detecting two pulses within a given coincidence window, no analysis of the shape or amplitude of the pulses would be required. This could lead to a significant simplification of the pulse processing system for a portable application.

Recent advances in plastic scintillators with a ^{6}Li loading hold promise for thermal and fast neutron spectroscopy applications. These plastics have the potential ability to discriminate between thermal neutron, fast neutron and gamma interactions [13]. Clearly separated away from gamma interactions in a typical PSD scatter plot, the thermal cluster can be as high as 470 keVee depending on the size and synthesis of materials used. The potential hazards of low-flashpoint liquid scintillators are not a problem with plastic scintillators and they become an attractive prospect for neutron dosimetry in mixed radiation fields. The ^{6}Li capture reaction is shown in equation 1.3.

$$^{1}n + ^{6}Li -> \ ^{3}H\ (2.73\ MeV) + ^{4}He\ (2.05\ MeV) \tag{1.3}$$

Comparing the isotopes of ^{6}Li (natural abundance approximately 8%) and ^{10}B (natural abundance approximately 20%), the later has a higher thermal capture cross section of 3837 barns compared to 940 barns with the former. Furthermore, when considering existing scintillators, ^{10}B-loaded liquid scintillators typically have 5% fractional mass loading of ^{10}B, compared to 0.1-0.3% of ^{6}Li-loaded plastic scintillators (developments to achieve higher loadings of ^{6}Li are ongoing [13]). Therefore, it is not known currently if capture gated neutron detection with a ^{6}Li-loaded plastic scintillator boasts any degree of thermal neutron detection efficiency.

This research investigates the suitability of capture gated detection of thermal neutrons in a ^{6}Li-loaded plastic scintillator. The thermal cluster as a result of neutron capture in a ^{6}Li scintillator lies within the fast neutron region. A novel technique is presented to perform thermal neutron assay based on removing the fast neutron background from this thermal neutron region.

2. Modelling neutron recoil distributions

A scintillator loaded with 0.14% fractional mass of ^{6}Li, measuring 40 mm diameter and 25 mm thickness, was considered in this work. This scintillator, plus a second with the same dimensions with 5% ^{10}B were modelled in a neutron field from a ^{241}AmBe radionuclide source to understand the mechanisms of capture gated detection within each of these scintillators.

The Monte Carlo radiation transport package, MCNP v5.0, was used to simulate the detectors [14]. In MCNP materials were simulated using the ENDF/B-VII.0 neutron cross section tables at temperature 293.13 K. To handle low energy thermal scattering of neutrons below 5 eV, MCNP has thermal treatment for a variety of material types. For s(α, β) thermal treatment, *poly.01t* was included in the MCNP input file. Using the particle tracking file (PTRAC), neutron recoil and neutron capture events within the scintillator were recorded. If an event resulted in a neutron capture,

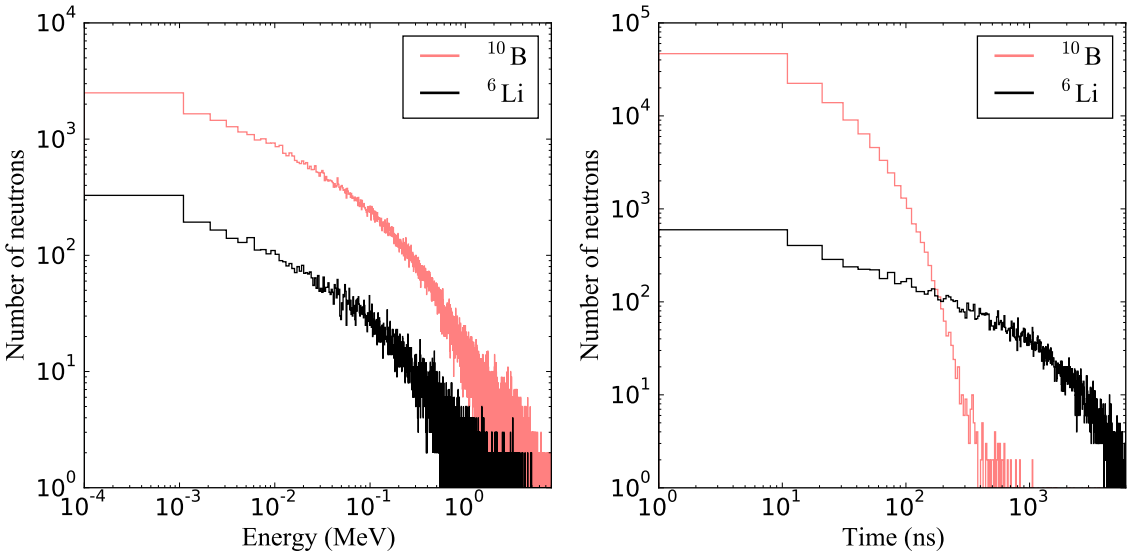

Figure 2. Simulated results of two different loading elements (^{6}Li and ^{10}B) in a scintillator. The figures show (a) a histogram of neutron energy deposited in the scintillator from an event resulting in neutron capture (b) a histogram of time between fast neutron interaction and capture of this neutron for a number of events.

the energy deposited in the scintillator was recorded. The time between the recoil and capture was also recorded.

The simulations were terminated after 4.4x10^{6} events that resulted in one or more proton recoils in the scintillator in each event. 119956 neutrons were captured in the ^{10}B scintillator and 13789 in the ^{6}Li-loaded scintillator. The differences in capture efficiency are reflected Figure 2a, showing a histogram of the energy deposited in the scintillator by each event before capture. Figure 2b shows a histogram of time between last recoil and capture. It can be seen that with the ^{10}B-loaded scintillator all neutrons were captured within 1 μs. This is in contrast to the ^{6}Li-loaded scintillator where the time to capture extends up to 6 μs. These results highlight that, as would be expected, with a significantly lower neutron capture cross-section and fractional mass content, the ^{6}Li-loaded scintillator has a much lower capture detection efficiency.

These simulations highlight a number of practical issues which must be considered with capture gating [15]. Due to their inherent properties, with any processing electronics and photomultiplier tube (PMT), a dead time will usually be imposed. Therefore, the pulse processing hardware and algorithms must capable of processing two pulses in quick succession. Figure 2b shows that for both ^{10}B and ^{6}Li, a high number of neutron captures occur less than 100 ns after a neutron recoil event. Also of consideration, it can be seen in Figure 2a a high number of recoils deposit less than 200 keV in the scintillator. Performing pulse shape discrimination on a detected signal with such low energy would be highly improbable. Therefore all gated events would need to be considered by the detection system. Furthermore, in a radiation field with a high gamma to neutron ratio, false triggering of the detection system from a gamma interaction would need to be considered. The higher the trigger is set, the lower the neutron capture detection efficiency. However, the lower this

trigger is set, the system must be able to cope with this high throughput demand.

3. Methodology

3.1 Experimental details

Two ^{6}Li-loaded scintillators were investigated in this experimental work. Both samples were provided by Lawrence Livermore National Laboratory (LLNL), USA [13]. Sample one, (denoted by the LLNL number 9023) measured 40 mm diameter and 25 mm thick. The second sample measured 25 mm in diameter by 18 mm thick, (denoted by the LLNL number 9038).

The scintillator was coupled to an ET Enterprises 9214B PMT with Eljen EJ550 optical grease. It was then enclosed in a light proof housing. The PMT was housed in an ET Enterprises B2F/RFI housing with a C638B tapered distribution voltage divider. The high voltage was set to -1200 V and connected to the PMT cathode. The PMT anode was connected to an Analog Devices AD9254 150 Msps, 14 bit analogue-to-digital converter (ADC). Each digitised ADC sample was clocked to an Altera Cyclone IV EP4CE115 field-programmable gate array (FPGA).

Within the FPGA, when the sampled ADC value passed over a set threshold, a 'first in first out' (FIFO) buffer was enabled. This sample and the subsequent 27 samples after this trigger, as well as one sample before the trigger, were clocked through the FIFO. When the FIFO was full, a universal asynchronous receiver/transmitter (UART) read the FIFO and sent these 29 samples from the FPGA to a PC through a USB link. This UART was configured to run at 8 Mbits per second. For each detected pulse, a message of 29 ADC samples and time stamp took approximately 200 μS to send. This allowed a throughput of around 4000 pulses per second. If a second pulse was detected before the first was cleared from the FIFO, data were clocked to a second parallel FIFO. A simplified block diagram of the electronic detector system is shown in Figure 3. Although a 150 Msps, 14 bit ADC is reasonably slow compared to current state-of-the-art, it is worth noting all work carried out and presented by LLNL in their research was undertaken with a 200 Msps 14 bit ADC system [13]. The raw ADC samples were recorded on a PC for offline analysis. The processing of the raw ADC samples was performed by a custom program written in Python using the charge comparison method [16].

With the use of Bonner spheres as a variable source moderation, a number of differing neutron fields were synthesised using three radionuclide sources; ^{241}AmBe, ^{241}AmLi and ^{252}Cf. The ^{241}AmBe and ^{252}Cf sources were each covered with two different sizes of HDPE sphere of diameters 12.7 cm and 20.32 cm. With the ^{241}AmBe source, the detector was placed 75 cm from the source; a distance of 147.2 cm was used for ^{241}AmLi and 72.4 cm for ^{252}Cf. These distances were selected to ensure that the throughput of the detector remained below 4000 pulses per second. A Pb cap surrounded all sources, excluding the ^{241}AmLi source (owing to its size), to suppress low energy gamma detections in the scintillator.

3.2 Charge comparison method (CCM)

The charge comparison method was used in this work to discriminate neutron and gamma interactions. The long integral was found by summing all 32 ADC samples. A number of short integrals were investigated and a value was chosen as 9 samples after the peak to the end of the data packet

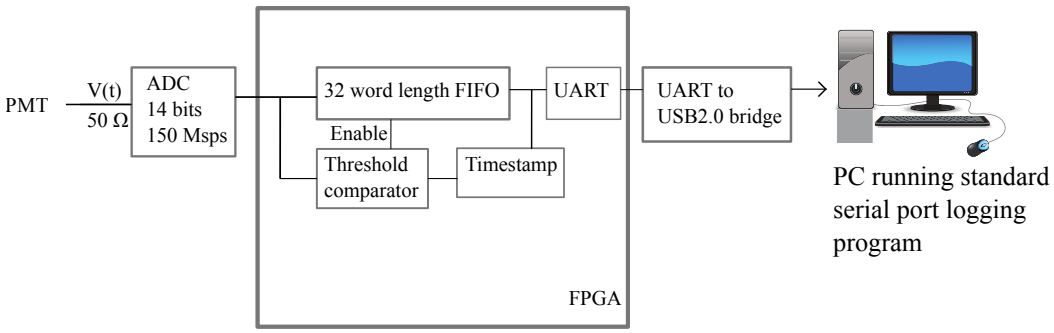

Figure 3. Block diagram of the detector system.

for each pulse. An example of the results observed for ^{241}AmBe with a 20.32 cm HDPE sphere around the source can be seen in Figure 4.

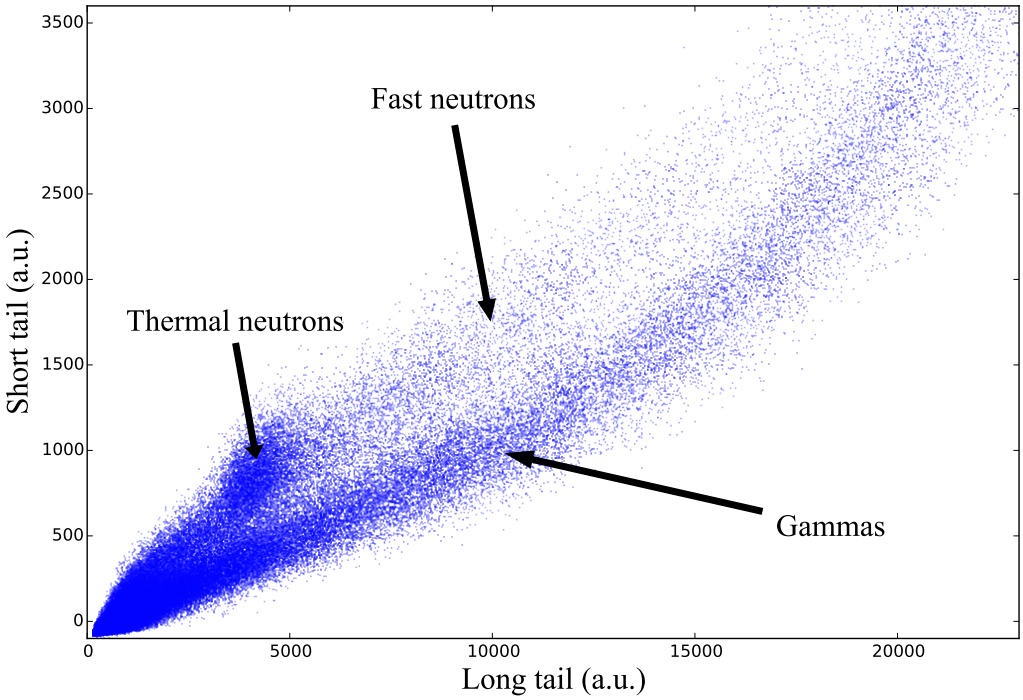

Figure 4. Pulse shape discrimination results from charge comparison method using ^{241}AmBe with a 20.32 cm sphere surrounding the source.

3.3 Separating neutrons from gamma

Traditionally, following pulse shape discrimination (PSD), a line of separation is placed on a PSD scatter plot to classify events as either a neutron or a gamma [17]. With liquid scintillators, such as BC501A, excellent neutron/gamma separation is observed and a line of separation is sufficient to classify these events. However, Figure 4 shows that placing a line of separation becomes a more onerous task.

Figure 5 shows a histogram of long/short integral ratios for pulse heights in the range of 3000 to 15000, resulting from ^{241}AmBe with a 20.32 cm sphere surrounding the source. Typically, neutron and gamma pulse shape variations for a given pulse height, follow a Gaussian distribution. However, it can be seen in Figure 5 that the neutron and gamma regions overlap. A line of separation could be placed at the intersection of the neutron and gamma distributions (discrimination index of 0) in Figure 5. However, it can clearly be seen that this would lead to events being incorrectly classified, as the Gaussian distributions overlap. In this case, resulting in an underestimate of the neutron fluence.

A Gaussian mixtures model (GMM) can be used to estimate the contributing Gaussian distributions which result in an observed distribution [18] [19]. Using an iterative algorithm, expectation-maximisation, the maximum likelihood parameters of the two Gaussian distributions are found. The GMM within the Python library *scikit-learn* was used to fit two Gaussian distributions shown in red in Figure 5. In this work it is assumed that the number of neutrons is equal to the integral of the fit performed by the GMM algorithm for the neutron Gaussian (the rightmost distribution). The GMM algorithm was applied to pulse heights in the region of 2000-3000 and secondly 3000-15000. The individual counts were summed to find the total neutron count (above the pulse height threshold of 2000).

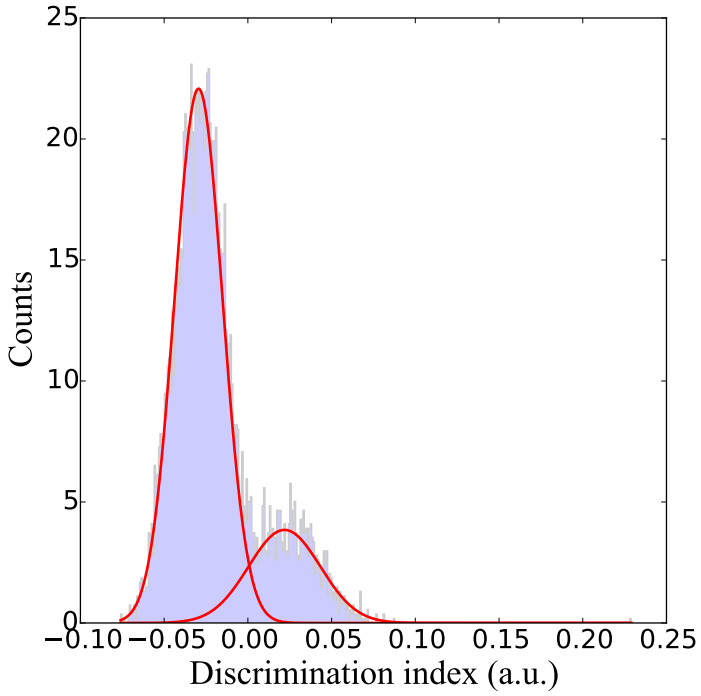

Figure 5. Filled histogram of pulse heights in the range 3000 to 15000 for 200 different discrimination indices using a ^{241}AmBe with a 20.32 cm sphere surrounding the source. The estimated fits for these distributions are shown in red. The left-hand distribution is the gamma pulses and right-hand neutron pulses.

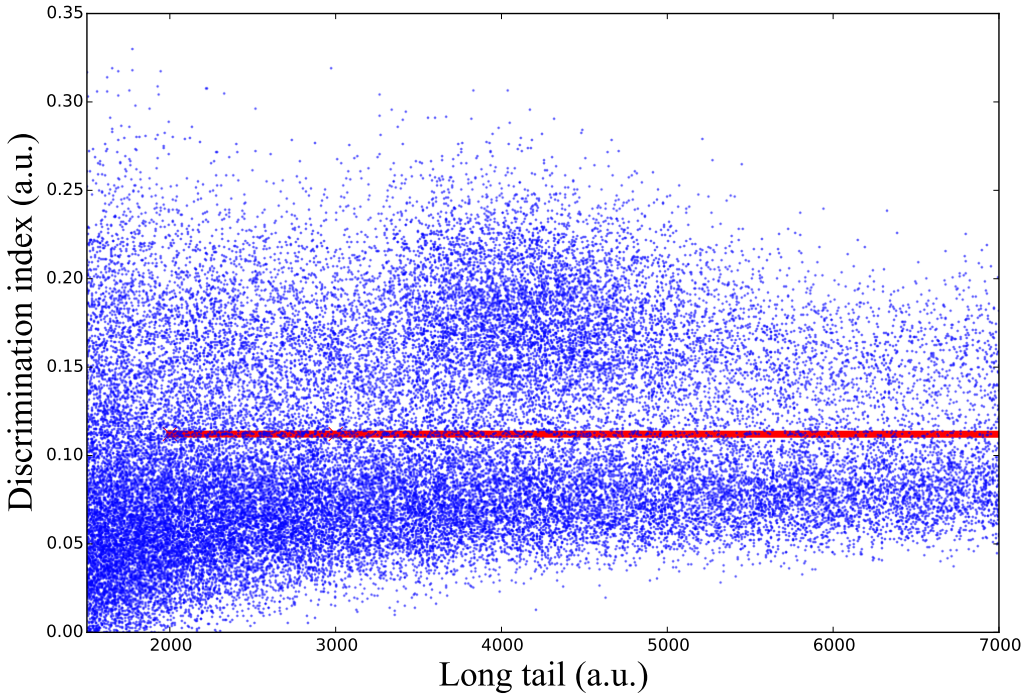

Figure 6. PSD scatter plot using ^{241}AmBe with a 20.32 cm sphere surrounding the source. This plot is limited to show just the thermal cluster region. The red line is the line of best separation found using the GMM algorithm. This separation is then used to find an approximate neutron pulse height spectrum. See text for further explanation.

3.4 Thermal neutron assay

With the ^{6}Li scintillator studied in this research, the thermal neutron cluster lies within the fast neutron plume. Using the LLNL smaller scintillator (number 9038), the cluster of thermal neutrons can clearly be seen in Figure 4 at around 4500,1000.

The statistical method outlined in the previous section detailing fast neutron assay cannot classify individual events as being neutron or gamma interactions. Therefore, to plot an approximate neutron pulse height spectrum, a line of separation was used. As previously discussed, this line of separation will mean misclassification of some events due to the overlapping Gaussian fits observed in Figure 5. However, for the purposes of performing the thermal neutron assay this does not matter. The mid-point of the two pulse height distributions found by the GMM algorithm (for example at discrimination index 0.0 in Figure 5) was used to find a marker for the separation between neutron and gamma events. The resulting PSD scatter plot with this line of separation (shown in red) is shown in Figure 6.

A plot of the resulting neutron pulse height spectrum can be seen in Figure 7, with the spectrum shown as a solid black line. The thermal cluster can be clearly seen between pulse heights of 3000 and 6000. In this work it was proposed that by applying a line of best fit to the data outside of the bound of the thermal cluster, a fit for the data without this thermal peak could be obtained. This was performed by applying a polynomial fit to the data outside of the bounds of 3000 to 6000, the resulting fit is shown in Figure 7 as a dashed red line. Within the bounds of the pulse heights

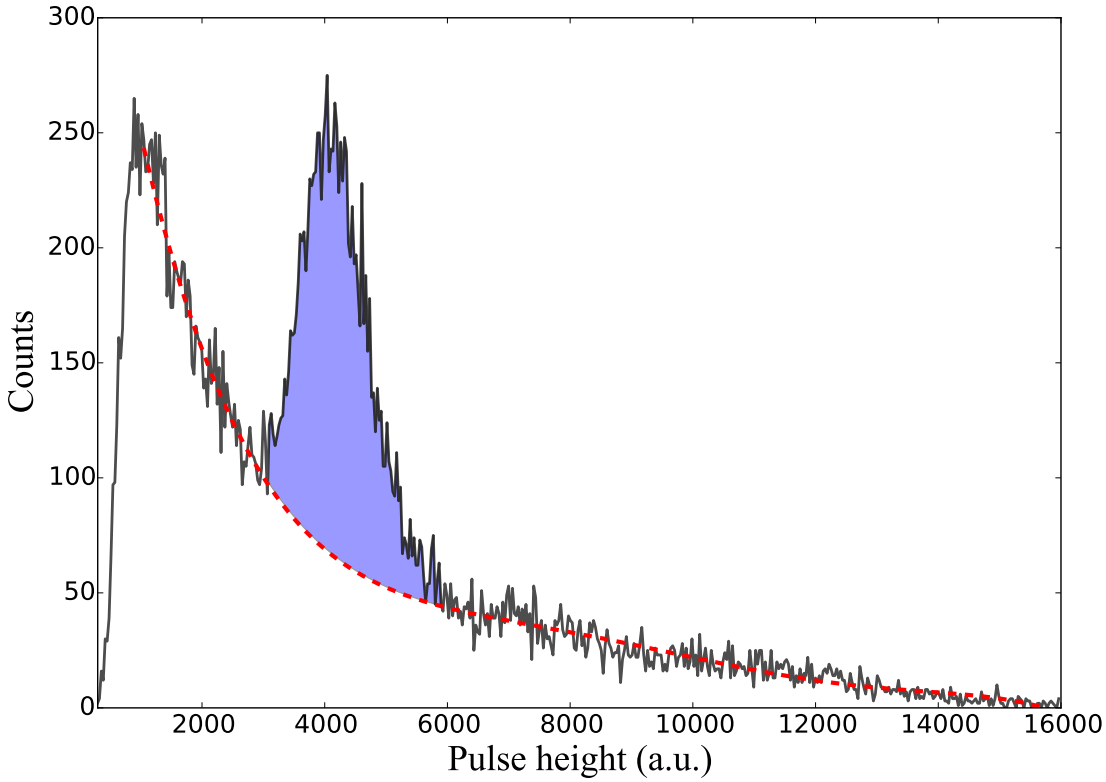

Figure 7. Neutron recoil pulse height with a ^{241}AmBe source with a 20.32 cm Bonner sphere around the source. The shaded blue area denotes the thermal neutrons. The dashed red line is the line of best fit for the recoil pulse height with the thermal neutrons removed.

found in the thermal cluster, the total integral was subtracted from the integral of the polynomial fit. This number was then taken to be the number of thermal neutrons and is shown in the blue shaded region in Figure 7. Having the highest thermal content in the fields studied in this work, the limits for the upper and lower bound of the thermal cluster were found using the ^{241}AmBe with a 20.32 cm diameter HDPE (Bonner) sphere around the source field. These upper and lower limits were then fixed at pulse heights 3096 and 5927 for the remainder of the experiments.

4. Results

4.1 Capture gating

The larger of the two ^{6}Li-loaded plastic scintillators (serial number 9023) was exposed to a bare ^{241}AmBe source and 5634859 events triggered the FPGA during 16 hours exposure time. 4854168 were below the saturation level of the ADC and were accepted as valid events for further processing. The scatter plot for CCM on the data can be seen in Figure 8. The green events in the background represent an event for which a single trigger occurred and no further events were recorded within a 13 μs gated time window. Where two events occurred within the gated time window, the second of these two events is shown in red. The total number of gated events was 5220. It would be expected, if all these events were neutron captures, that the red dotes would cluster around the neutron capture

region of pulse heights between 3000 and 6000. However, it can be seen that a number of these events appear to have been gamma interactions. Regardless of the misclassification of these events, these experimental results are in the same order of magnitude as the simulations in the work.

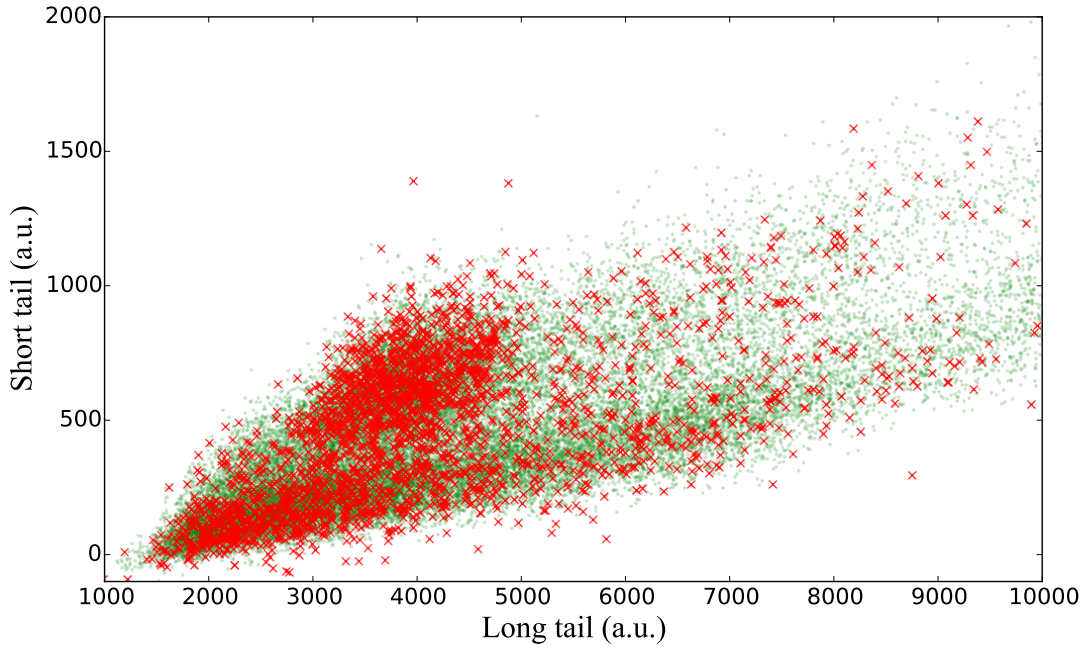

Figure 8. Pulse shape discrimination results from charge comparison method using a ^{241}AmBe source. Green events correspond to non-gated events, and red corresponds to the second pulse within a gated time window.

4.2 Thermal neutron assay

Seven neutron fields synthesised from three different sources were investigated in this work. Neutron recoil pulse height plots for a sample of the synthesised fields studied in this research are shown in Figure 9.

An ^{241}AmBe source with a 20.32 cm Bonner sphere around the source was used to synthesise a field with both fast neutrons and high thermal neutron content. Inspection of Table 1 shows that for this configuration, from 153033 triggered events, 21104 fast neutron interactions occurred and 7761 thermal neutrons were captured in the detector. This experiment was repeated and the repeatability of the algorithm was investigated for 105946 triggered events. The two ratio of fast to thermal neutrons for each experiment was 3.0 and 2.7, which is reasonably consistent.

A cadmium container was installed surrounding the front and sides of the detector to remove this thermal content from the field. The results are shown in Figure 9b. It can clearly be seen that the cadmium captures a significant number of the thermal neutrons, confirming that the presence of this peak is due to the thermal neutrons when no container is present. This is further compounded by the results shown in Figure 9d for an ^{241}AmBe field with no moderation, and hence, low thermal

Table 1. Table detailing the sources used with the two different sized scintillators in this work. Unless otherwise stated, Pb cap installed over each of the sources.

Source	Moderation	Additional Notes	Number of triggered events	Fast neutrons	Thermal neutrons	Fast to thermal neutron ratio
^{241}AmBe	20.32 cm Bonner sphere	Cd vessel	105813	16013	1073	14.9
^{241}Ambe	20.32 cm Bonner sphere		105946	14934	4942	3.0
^{241}Ambe	20.32 cm Bonner sphere		153033	21104	7786	2.7
^{241}AmBe	12.7 cm Bonner sphere		108535	22886	3467	6.6
^{241}AmBe	None		114720	30786	651	47.3
^{241}AmLi	12.7 cm Bonner sphere	No Pb cap	199910	0	1835	n/a
^{252}Cf	20.32 cm Bonner sphere		123410	4723	2619	1.8
^{252}Cf	12.7 cm Bonner sphere		122826	6471	1667	3.9
^{252}Cf	None		121018	10083	93	108.4

neutron content in the field. Figure 9c shows a neutron field of ^{252}Cf surrounded by a 20.32 cm Bonner sphere.

Table 1 shows all the results recorded in this research. Events with a pulse integral of 3000 (the lower limit of the thermal cluster) or greater are classified as a fast neutron. It can be seen that by surrounding the radionuclide source with Bonner spheres of increasing diameter up to 20.32 cm, a higher thermal neutron content in these fields is recorded.

The ^{241}AmLi surrounded by a 12.7 cm Bonner sphere field highlighted shortcomings in the GMM algorithm when applied to this technique. This field was specificially chosen to investigate performance of the technique in the presence of a high gamma, low neutron field. Figure 10 shows the PSD scatter plot recorded with 2x10^6 triggered events. It can be seen that the gamma/neutron ratio of this source was extremely high. With very few fast or thermal neutrons compared to the high gamma flux, the GMM algorithm predicts that the observed thermal events are gamma interactions. The thermal assay algorithm was adapted such that if the GMM algorithm estimated 1500 or fewer total neutron interactions, it resorted to a user-configured threshold between gamma and thermal neutrons. In this case, the fast neutron background was too low, and the number of events in the thermal neutron region was considered to be the thermal neutron count.

5. Conclusion

A new technique has been investigated for thermal neutron assay with a ^{6}Li-loaded plastic scintillator. Thermal neutron assay has been performed on 7 different neutron fields synthesised from ^{241}AmBe, ^{241}AmLi and ^{252}Cf radionuclide sources. This thermal assay was performed by removing the fast neutron background count within the pulse-height range of detected thermal neutrons. A statistical technique, Gaussian mixtures model, has been used to perform fast neutron assay with non-ideal neutron/gamma separation.

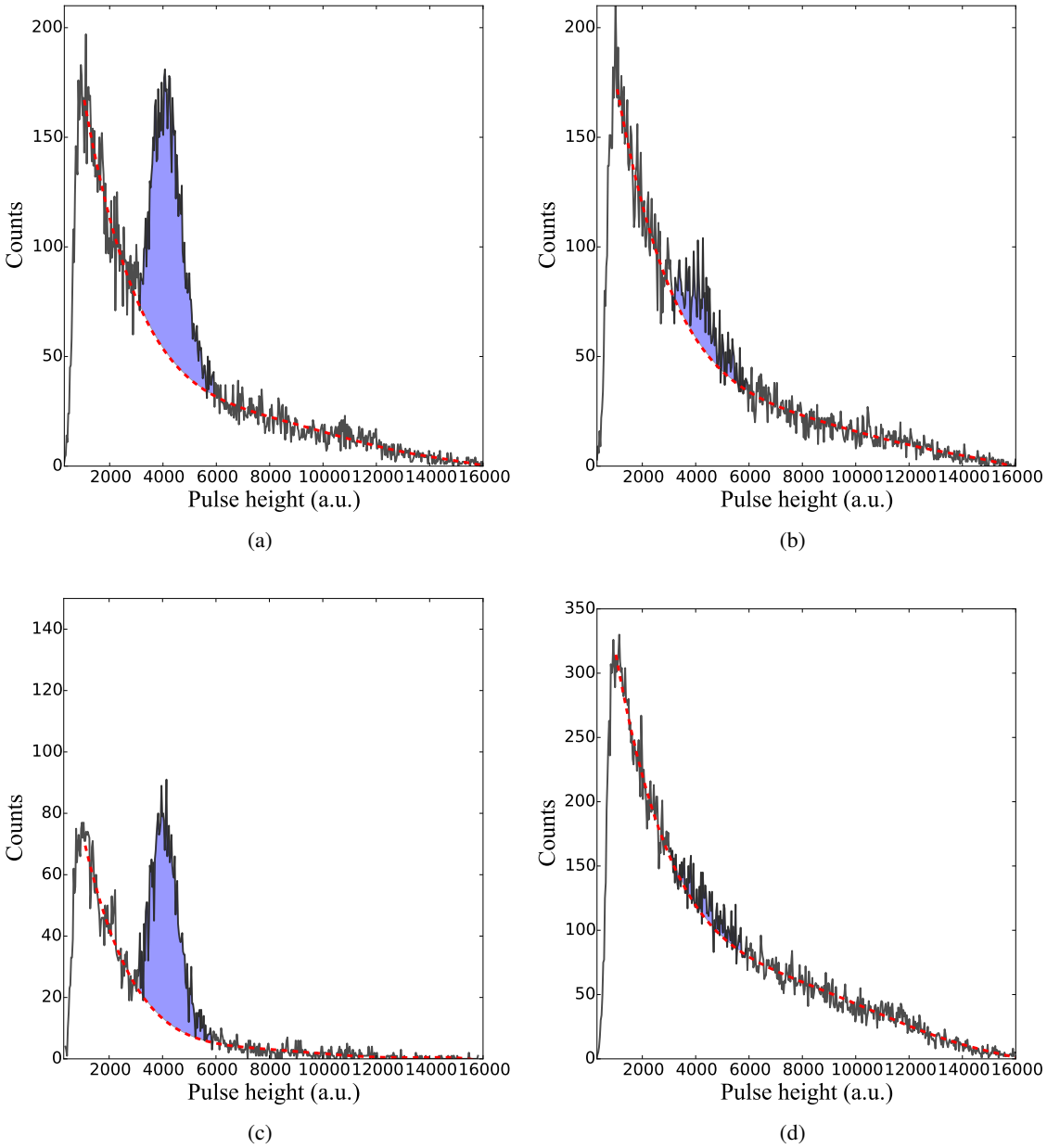

Figure 9. Neutron recoil pulse height, with shaded blue area denoting the thermal neutrons. The dashed red line is the line of best fit for the recoil pulse height with the thermal neutrons removed. Neutron fields for (a) ^{241}AmBe surrounded by a 20.32 cm Bonner sphere, (b) ^{241}AmBe surrounded by a 20.32 cm Bonner sphere and detector enclosed in a Cd vessel, (c) ^{252}Cf surrounded by a 20.32 cm Bonner sphere (d) ^{241}AmBe with no moderation.

Capture gated ^{10}B-loaded liquid scintillator detectors are an established thermal neutron detection technique. Simulations of one of these detectors with a ^{6}Li-loaded plastic scintillator were performed. When compared to ^{10}B, the lower neutron capture cross section and fractional mass content of ^{6}Li results in a low efficiency thermal neutron detector. Furthermore, it was observed

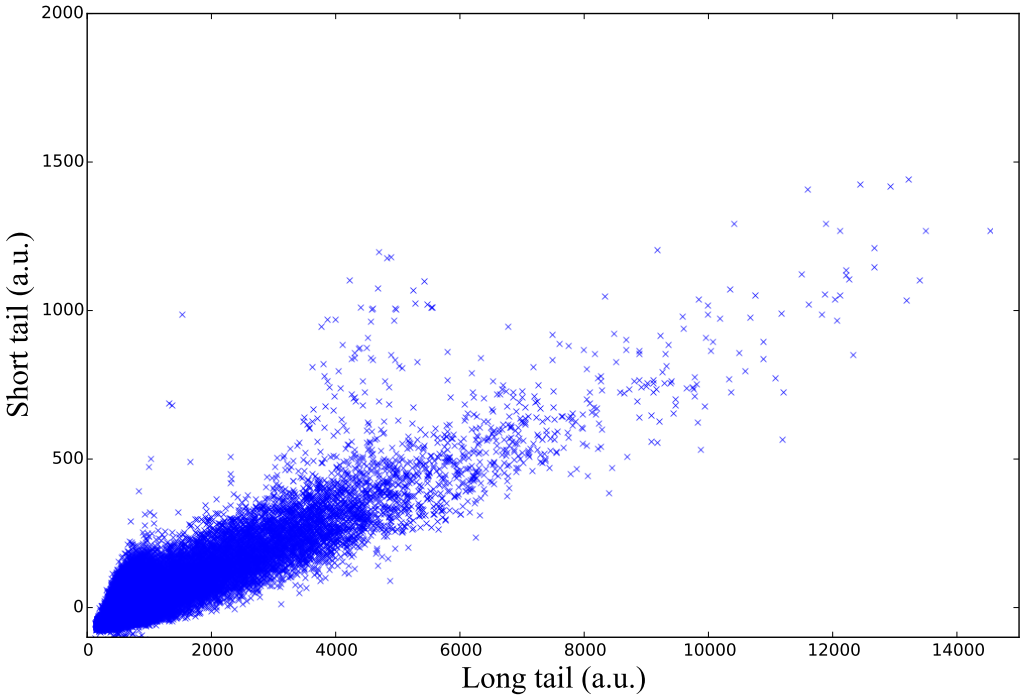

Figure 10. Pulse shape discrimination results from charge comparison method using a ^{241}AmLi source. A Pb cap did not surround the source in this experiment (owing to the size of the source) and as such a high gamma to neutron ration was observed in this field.

through experimental work that not all of the capture gated events were that of a signal found in the thermal neutron region of a PSD scatter plot. It was assumed these events outside this region were gamma interactions. Working in a high gamma, low neutron field would further hinder thermal neutron detection using this technique.

The algorithms are such that after calibration, no user input is required. The techniques described in this work have been successfully implemented as algorithms and tested on a number of different fields in this manner. The algorithms described lend themselves well to implementation into a portable real-time neutron detection system to perform neutron dosimetry.

The applicability of the techniques described in this research provide a method for performing both fast and thermal neutron assay beyond that solely of a ^{6}Li-loaded plastic scintillator. Scintillators for thermal neutron detection such as CLYC and ^{10}B-loaded plastic scintillators appear to be suitable to use this technique for fast and thermal neutron assay [20, 21].

Acknowledgments

The authors would like to express thanks to Natalia Zaitseva and the team at LLNL for providing the scintillator. The authors would like to acknowledge the funding support from EPSRC and National Physical Laboratory, Teddington, UK. The authors acknowledge the use of the package Matplotlib for all plots in this research [22]. The data generated in this work are available from the Lancaster University data archive [23].

References

[1] Y.H. Chen et al. Study of n-γ discrimination in low energy range (above 40 keVee) by charge comparison method with a BC501a liquid scintillation detector. *Chinese Physics C*, 38(3):036001, March 2014.

[2] R.A. Cecil et al. Improved predictions of neutron detection efficiency for hydrocarbon scintillators from 1 MeV to about 300 MeV. *Nuclear Instruments and Methods*, 161(3):439–447, 1979.

[3] F. Posny et al. Neutron spectrometry system for radiation protection: Measurements at work places and in calibration fields. *Radiation Protection Dosimetry*, 44(1-4):239–242, 1992.

[4] D.J. Thomas et al. An intercomparison of neutron field dosimetry systems. *Radiation Protection Dosimetry*, 44(1-4):219–222, 1992.

[5] P. Peerani et al. Testing on novel neutron detectors as alternative to ^{3}He for security applications. *Nuclear Instruments and Methods in Physics Research Section A: Accelerators, Spectrometers, Detectors and Associated Equipment*, 696:110–120, December 2012.

[6] S.D. Jastaniah et al. Digital techniques for n/γ pulse shape discrimination and capture-gated neutron spectroscopy using liquid scintillators. *Nuclear Instruments and Methods in Physics Research Section A: Accelerators, Spectrometers, Detectors and Associated Equipment*, 517(1-3):202–210, January 2004.

[7] S.A. Pozzi et al. Analysis of the response of capture-gated organic scintillators. *IEEE Transactions on Nuclear Science*, 52(6):3141–3146, December 2005.

[8] M. Flaska et al. Digital pulse shape analysis for the capture-gated liquid scintillator BC-523a. *Nuclear Instruments and Methods in Physics Research Section A: Accelerators, Spectrometers, Detectors and Associated Equipment*, 599(2-3):221–225, February 2009.

[9] P. Holm et al. A capture-gated neutron spectrometer for characterization of neutron sources and their shields. *Nuclear Instruments and Methods in Physics Research Section A: Accelerators, Spectrometers, Detectors and Associated Equipment*, 751:48–54, July 2014.

[10] F. Pino et al. Detecting fast and thermal neutrons with a boron loaded liquid scintillator, EJ-339a. *Applied Radiation and Isotopes*, 92:6–11, September 2014.

[11] L. Swiderski et al. Boron-10 Loaded BC523a Liquid Scintillator for Neutron Detection in the Border Monitoring. *IEEE Transactions on Nuclear Science*, 55(6):3710–3716, December 2008.

[12] L. Swiderski et al. Further Study of Boron-10 Loaded Liquid Scintillators for Detection of Fast and Thermal Neutrons. *IEEE Transactions on Nuclear Science*, 57(1):375–380, February 2010.

[13] N. Zaitseva et al. Pulse shape discrimination with lithium-containing organic scintillators. *Nuclear Instruments and Methods in Physics Research Section A: Accelerators, Spectrometers, Detectors and Associated Equipment*, 729:747–754, November 2013.

[14] A General Monte Carlo N-Particle Transport Code, Version 5.

[15] N.S. Bowden et al. A note on neutron capture correlation signals, backgrounds, and efficiencies. *Nuclear Instruments and Methods in Physics Research Section A: Accelerators, Spectrometers, Detectors and Associated Equipment*, 693:209–214, November 2012.

[16] T.K. Alexander et al. An amplitude-insensitive system that distinguishes pulses of different shapes. *Nuclear Instruments and Methods*, 13(0):244 – 246, 1961.

[17] K.A.A. Gamage et al. A comparison of four different digital algorithms for pulse-shape discrimination in fast scintillators. *Nuclear Instruments and Methods in Physics Research Section A: Accelerators, Spectrometers, Detectors and Associated Equipment*, 642(1):78–83, June 2011.

[18] C.M. Bishop. *Pattern recognition and machine learning*. Information science and statistics. Springer, New York, 2006.

[19] A.P. Dempster et al. Maximum Likelihood from Incomplete Data via the EM Algorithm. *Journal of the Royal Statistical Society. Series B (Methodological)*, 39(1):1–38, 1977.

[20] I.A. Pawełczak et al. Boron-loaded plastic scintillator with neutron-γ pulse shape discrimination capability. *Nuclear Instruments and Methods in Physics Research Section A: Accelerators, Spectrometers, Detectors and Associated Equipment*, 751:62–69, July 2014.

[21] C.M. Whitney et al. Gamma-neutron imaging system utilizing pulse shape discrimination with CLYC. *Nuclear Instruments and Methods in Physics Research Section A: Accelerators, Spectrometers, Detectors and Associated Equipment*, 784:346–351, June 2015.

[22] J.D. Hunter. Matplotlib: A 2D Graphics Environment. *Computing in Science and Engineering*, 9(3):90–95, 2007.

[23] M.J.I Balmer et al. doi:10.17635/lancaster/researchdata/7.